Commun Nonlinear Sci Numer Simulat 68 (2019) 15–30

Contents lists available at ScienceDirect

Commun Nonlinear Sci Numer Simulat

journal homepage: www.elsevier.com/locate/cnsns

Research paper

High-performance implementation of a Runge–Kutta finite-difference scheme for the Higgs boson equation in the de Sitter spacetime

Andras Balogh*, Jacob Banda, Karen Yagdjian

The University of Texas Rio Grande Valley, Edinburg, TX 78539, United States

ARTICLE INFO

Article history:
Received 4 March 2018
Revised 7 July 2018
Accepted 9 July 2018
Available online 30 July 2018

Keywords:
Higgs boson equation in the de Sitter spacetime
High-performance computations
Unforced damped Duffing equations

ABSTRACT

High performance computations are presented for the Higgs boson equation in the de Sitter Spacetime using explicit fourth order Runge–Kutta scheme on the temporal discretization and fourth order finite difference discretization in space. In addition to the full, $(3+1)-$dimensional equation we also examine the $(1+1)-$dimensional radial solutions. The numerical code for the $(3+1)-$dimensional equation is programmed in CUDA Fortran and is performed on NVIDIA Tesla K40c GPU Accelerators. The radial form of the equation is simulated in MATLAB. The numerical results demonstrate the existing theoretical result that under certain conditions bubbles form in the scalar field. We also demonstrate the known blow-up phenomena for the solutions of the related semilinear Klein–Gordon equation with imaginary mass. Our numerical studies suggest several previously not known properties of the solution for the Higgs boson equation in the de Sitter spacetime for which theoretical proofs do not exist yet: 1. smooth solution exists for all time if the initial conditions are compactly supported and smooth; 2. under some conditions no bubbles form; 3. solutions converge to step functions related to unforced, damped Duffing equations.

1. Introduction

There are several open mathematical questions about the Higgs boson in the de Sitter spacetime. We are interested in the feature of this issue related to the theory of partial differential equations and, especially, to the problem of the global-in-time existence of the solution. In fact, the equation is semilinear since it contains the Higgs potential and has time dependent coefficient. Because of the lack of mathematically rigorous proof for the existence of global-in-time solution we turn to numerical investigations which can shed light on that issue, and can also indicate the creation of so-called bubbles. In order to achieve that aim, in this article we perform high-performance numerical computations using Graphical Processing Units for examining the behavior of solutions to the Higgs boson equation in the de Sitter spacetime.

The Klein–Gordon equation with the Higgs potential (the Higgs boson equation) in the de Sitter spacetime can be written as

$$\phi_{tt} - e^{-2t}\Delta\phi + 3\phi_t = \mu^2\phi - \lambda\phi^3, \tag{1}$$

---

* Corresponding author.
E-mail address: andras.balogh@utrgv.edu (A. Balogh).

https://doi.org/10.1016/j.cnsns.2018.07.011

$$\phi(\vec{x},0)=\varphi_0(\vec{x}), \quad \vec{x}\in\mathbb{R}^3, \tag{2}$$

$$\phi_t(\vec{x},0)=\varphi_1(\vec{x}), \quad \vec{x}\in\mathbb{R}^3. \tag{3}$$

Here Δ is the Laplace operator in $\vec{x}\in\mathbb{R}^3$, $t>0$ is the time variable, the parameters are $\lambda>0$ and $\mu>0$, while $\phi=\phi(\vec{x},t)$ is a real-valued function. From now on we consider solution $\phi=\phi(\vec{x},t)$ to the Klein-Gordon equation which is at least continuous. It is of considerable interest for particle physics and inflationary cosmology to study the so-called bubbles [8,21,29]. In the quantum field theory a bubble is defined as a simply connected domain surrounded by a wall such that the field approaches one of the vacuums outside of a bubble (see, e.g., [8]). It is mathematically reasonable to define the bubble as a maximal connected set of spatial points $\vec{x}\in\mathbb{R}^3$ at which solution to the Cauchy problem (1)–(3) changes sign.

First we discuss the existence of global-in-time solution of some other special cases of the more general equation

$$\phi_{tt}-e^{-2t}\Delta\phi+n\phi_t=\mu^2\phi-F(\phi), \tag{4}$$

where $F(\phi)=\pm\phi^p$ or $F(\phi)=\pm|\phi|^{p-1}\phi$, or some more general function, and $\vec{x}\in\mathbb{R}^n$. For this equation the local existence of solution in different spaces of functions is well investigated for appropriate values of p and n. The estimate for the lifespan of the solution is given as follows. The main parameter that controls estimates and solvability is the principal square root $M:=(\mu^2+n^2/4)^{\frac{1}{2}}$. Let $H^s(\mathbb{R}^n)=W^{s,2}(\mathbb{R}^n)$ be the usual Sobolev space [1]. The function F is said to be Lipschitz continuous with exponent $\alpha\ge 0$ in the space $H^s(\mathbb{R}^n)$ if there is a constant $C\ge 0$ such that

$$\|F(\phi_1(x))-F(\phi_2(x))\|_{H^s(\mathbb{R}^n)}\le C\|\phi_1-\phi_2\|_{H^s(\mathbb{R}^n)}\left(\|\phi_1\|^{\alpha}_{H^s(\mathbb{R}^n)}+\|\phi_2\|^{\alpha}_{H^s(\mathbb{R}^n)}\right) \tag{5}$$

for all $\phi_1,\phi_2\in H^s(\mathbb{R}^n)$. Assume that the nonlinear term $F(u)$ is Lipschitz continuous in the space $H^s(\mathbb{R}^n)$, $s>n/2\ge 1$, $F(0)=0$, $\alpha>0$ and $M\in\mathbb{C}$. According to (iii) of Theorem 0.1 from [32] we have the following statement: *If* $\mu>0$, *then the lifespan* T_{ls} *of the solution can be estimated from below as follows:*

$$T_{ls}\ge -\frac{1}{M-\frac{n}{2}}\ln\left(\|\varphi_0\|_{H^s(\mathbb{R}^n)}+\|\varphi_1\|_{H^s(\mathbb{R}^n)}\right)-C(m,n,\alpha)$$

with some constant $C(m, n, \alpha)$ *for sufficiently small* $\|\varphi_0\|_{H^s(\mathbb{R}^n)}$ *and* $\|\varphi_1\|_{H^s(\mathbb{R}^n)}$. In particular, this covers the cases

$$F(\phi)=\pm|\phi|^{\alpha}\phi; \qquad F(\phi)=\pm|\phi|^{\alpha+1}; \quad \text{and} \quad F(\phi)=\lambda\phi^3.$$

For the function $u=e^{\frac{n}{2}t}\phi$ Eq. (4) leads to

$$u_{tt}-e^{-2t}\triangle u-M^2u=-e^{\frac{n}{2}t}F\left(e^{-\frac{n}{2}t}u\right) \tag{6}$$

with $M\ge n/2$. The last equation can be regarded as a Klein–Gordon equation whose squared physical mass $m^2=-M^2$ is negative. The quantum fields whose squared physical masses are negative (imaginary mass) represent tachyons (see, e.g., [4]). According to [4] the free tachyons in the Minkowski spacetime have to be rejected on stability grounds since the localized disturbances of the Klein-Gordon equation with imaginary mass spread with at most the speed of light, but grow exponentially.

Epstein and Moschella in [13] give a complete study of a family of scalar tachyonic quantum fields which are linear Klein-Gordon quantum fields on the de Sitter manifold whose squared masses are negative

$$\phi_{tt}-e^{-2t}\Delta\phi+n\phi_t+m^2\phi=0\,, \tag{7}$$

and take an infinite set of discrete values $m^2=-k(k+n)$, $k=0,1,2,\ldots$. The nonexistence of a global-in-time solution of the semilinear Klein-Gordon massive tachyonic (self-interacting quantum fields) equation in the de Sitter spacetime, that is a finite lifespan, is proved in [30]. In fact, Theorem 1.1 in [30] states that if $c\ne 0$, $\alpha>0$, and $m\ne 0$, then for every positive numbers ε and s there exist functions φ_0, $\varphi_1\in C_0^{\infty}(\mathbb{R}^n)$ such that $\|\varphi_0\|_{H^s(\mathbb{R}^n)}+\|\varphi_1\|_{H^s(\mathbb{R}^n)}\le\varepsilon$ but the solution $\phi=\phi(x,t)$ of the semilinear equation

$$\phi_{tt}-e^{-2t}\Delta\phi+n\phi_t-m^2\phi=c|\phi|^{1+\alpha}\,, \tag{8}$$

with the initial values $\phi(\vec{x},0)=\varphi_0(\vec{x})$, $\phi_t(\vec{x},0)=\varphi_1(\vec{x})$, blows up in finite time. This would also imply the blowup of the *sign-preserving* solutions (under some additional conditions) of the equation

$$\phi_{tt}-e^{-2t}\Delta\phi+n\phi_t-m^2\phi=-|\phi|^{\alpha}\phi\,. \tag{9}$$

While the above special cases of Eq. (4) demonstrate that finite-time blow-up of solutions occurs sometimes and other times solutions exist globally in time, the issue of the existence of a global-in-time of solution of our specific Eq. (1) is still an open problem.

There have been numerous numerical approaches for solving the various types of nonlinear Klein–Gordon equations and other nonlinear wave equations. Most of the existing numerical results are for one space dimension, including a cubic B-spline collocation method presented in [25]; the Adomian decomposition method involving a Klein–Gordon equation and solitary waves in [18]; and the method of lines in one space dimensions used in [15] for the mth-order Klein–Gordon equation. In the computational analysis of nonlinear hyperbolic equations it is important to preserve not just the dissipation of energy (see [22]) but to minimize the dispersion error as well (see [5]). Explicit methods, even though they are only conditionally stable, have a tendency to have smaller dispersion error compared to the usually unconditionally stable implicit methods. Comparison of several explicit finite difference schemes have been presented for the one spatial variable case in [17]. A differential transform method with variational iteration method with Adomian' s polynomials was presented for the Higgs boson equation in de Sitter Spacetime in [33]. The Adomian decomposition method was also used for the Klein–Gordon equation with quadratic nonlinearity in [3] with a general method presented for the $(3+1)-$dimensional case and an example with a known solution presented for a $(1+1)-$dimensional case. Even in higher spatial dimensions if one uses radial basis functions the resulting problem becomes one-dimensional (see [10] and [12]). In [9] a fourth-order compact scheme was introduced and numerically tested for a nonlinear Klein–Gordon equation in one space dimension. With a simple unit cube for the computation domain we chose a finite difference discretization with fourth order of accuracy for the spatial component along with a matching fourth-order Runge–Kutta method for the time variable. The resulting explicit numerical code (stencil code) is very well suited for high performance computations using Graphical Processing Units. We refer the reader to [28] regarding the development of Runge–Kutta methods for partial differential equation. In Section 2 we describe the numerical approach for the $(3+1)-$dimensional general case as well as for $(1+1)-$dimensional radial solutions. In Section 3 the main computational results are presented via various examples in order to test the numerical code and to examine the properties of solutions to the Higgs boson equation in the de Sitter spacetime. Finally in Section 4 conclusions are given in the form of conjectures.

2. The numerical method

Our numerical approach uses a fourth order finite difference method in the three-dimensional space in combination with an explicit fourth order Runge–Kutta method in time for the discretization and numerical solution of the Higgs boson equation in the de Sitter spacetime. In addition to the general case of three spatial dimensions we also investigate radial solutions in one spatial dimension, which is much less demanding computationally. In this section we describe these choices of approach.

2.1. General 3D solutions

We only consider solutions of the Higgs boson Eq. (1) with compact support in space. Since the solution has the finite speed of propagation e^{-t} (see, e.g., [16]), the total distance travelled by the solution is $\int_0^\infty e^{-t}dt = 1$. The finite cone of influence along with a rescaling of the spatial domain enables us to use zero boundary conditions on the unit box $\Omega = [0,1]\times[0,1]\times[0,1]$ as computational domain. The rescaled Higgs boson equation then has the form

$$\phi_{tt} - \frac{1}{L^2}e^{-2t}\Delta\phi + 3\phi_t = \mu^2\phi - \lambda\phi^3, \quad \vec{x}\in\Omega, \quad t\in(0,T], \tag{10}$$

$$\phi(\vec{x},0) = \varphi_0(\vec{x}), \quad \vec{x}\in\Omega, \tag{11}$$

$$\phi_t(\vec{x},0) = \varphi_1(\vec{x}), \quad \vec{x}\in\Omega, \tag{12}$$

$$\phi(\partial\Omega,t) = 0, \quad t\in[0,T]. \tag{13}$$

Here we set the initial condition to have compact support inside Ω and choose $L>0$ large enough so that information propagating from the initial compact support will never reach the boundary of the unit box. Since the solution will be zero on continuous regions outside the compact support, we use finite difference method for spatial discretization, which is a local approach as opposed to global approaches like spectral methods. A uniform grid is chosen in all three space variables with grid spacing $\delta x = \delta y = \delta z = 1/n$ with $n\in\mathbb{N}$ and with notation

$$\phi_{jkl}(t) = \phi\big(x_j, y_k, z_l, t\big) = \phi(j\delta x,\ k\delta y,\ l\delta z,\ t).$$

for $t\in[0,T]$. From now on the subscript jkl will mean varying indices $j,k,l = 0,1,\dots,n$. The second partial derivatives in the Laplacian $\Delta\phi = \frac{\partial^2\phi}{\partial x^2} + \frac{\partial^2\phi}{\partial y^2} + \frac{\partial^2\phi}{\partial z^2}$ are discretized using the fourth-order central difference scheme (see, e.g., [19])

$$\begin{aligned}
\left.\frac{\partial^2\phi}{\partial x^2}\right|_{jkl} &= \frac{1}{\delta x^2}\Big(-\frac{1}{12}\phi_{j-2,kl} + \frac{4}{3}\phi_{j-1,kl} - \frac{5}{2}\phi_{jkl} + \frac{4}{3}\phi_{j+1,kl} - \frac{1}{12}\phi_{j+2,kl}\Big) + O\big(dx^4\big),\\
\left.\frac{\partial^2\phi}{\partial y^2}\right|_{jkl} &= \frac{1}{\delta y^2}\Big(-\frac{1}{12}\phi_{jk-2,l} + \frac{4}{3}\phi_{jk-1,l} - \frac{5}{2}\phi_{jkl} + \frac{4}{3}\phi_{jk+1,l} - \frac{1}{12}\phi_{jk+2,l}\Big) + O\big(dy^4\big),\\
\left.\frac{\partial^2\phi}{\partial z^2}\right|_{jkl} &= \frac{1}{\delta z^2}\Big(-\frac{1}{12}\phi_{jkl-2} + \frac{4}{3}\phi_{jkl-1} - \frac{5}{2}\phi_{jkl} + \frac{4}{3}\phi_{jkl+1} - \frac{1}{12}\phi_{jkl+2}\Big) + O\big(dz^4\big).
\end{aligned}$$

We also transform Eq. (10) into a first-order-in-time system of two equations via notations

$$\vec{v}(t)=\begin{pmatrix}\vec{v}_1\\ \vec{v}_2\end{pmatrix}(t)=\begin{pmatrix}\vec{\phi}_{jkl}\\ \frac{\partial}{\partial t}\vec{\phi}_{jkl}\end{pmatrix}(t) \tag{14}$$

and

$$\vec{f}(t,\vec{v}(t))=\begin{pmatrix}\vec{v}_2\\ -3\vec{v}_2+\frac{e^{-2t}}{L^2}\Delta\vec{v}_1+\mu^2\vec{v}_1-\lambda\vec{v}_1^3\end{pmatrix}, \tag{15}$$

where $\vec{v}_1=\vec{\phi}_{jkl}=(\phi_{000},\dots,\phi_{nnn})^T$. This way we obtain an evolution system of the form

$$\frac{d}{dt}\vec{v}(t)=\vec{f}(t,\vec{v}(t)) \tag{16}$$

with initial and boundary conditions

$$\begin{aligned}&\vec{v}(\vec{x},0)=\begin{pmatrix}\vec{\varphi}_{0_{jkl}}\\ \vec{\varphi}_{1_{jkl}}\end{pmatrix}(\vec{x}),\quad \vec{x}\in\Omega,\\ &\vec{v}(\partial\Omega,t)=\vec{0},\quad t\in[0,T].\end{aligned}$$

Note that the second component of the right-hand-side function (15) has the form

$$\begin{aligned}(f_2)_{jkl}&=\mu^2(v_1)_{jkl}-\lambda(v_1)_{jkl}^3-3(v_2)_{jkl}+\frac{e^{-2t}}{L^2}\Delta(v_1)_{jkl}\\ &=\left(\mu^2-\frac{15}{2}\frac{e^{-2t}}{L^2\delta x^2}\right)(v_1)_{jkl}-\lambda(v_1)_{jkl}^3-3(v_2)_{jkl}\\ &\quad-\frac{1}{12}\frac{e^{-2t}}{L^2\delta x^2}\big((v_1)_{jkl+2}+(v_1)_{jkl-2}+(v_1)_{jkl+2n}+(v_1)_{jkl-2n}+(v_1)_{jkl+2n^2}+(v_1)_{jkl-2n^2}\big)\\ &\quad+\frac{4}{3}\frac{e^{-2t}}{L^2\delta x^2}\big((v_1)_{jkl+1}+(v_1)_{jkl-1}+(v_1)_{jkl+n}+(v_1)_{jkl-n}+(v_1)_{jkl+n^2}+(v_1)_{jkl-n^2}\big).\end{aligned}$$

For time discretization we use the classical, explicit fourth-order Runge–Kutta method (see, e.g., [11])

$$\vec{v}(t+\delta t)=\vec{v}(t)+\frac{\vec{k}_1+2\vec{k}_2+2\vec{k}_3+\vec{k}_4}{6}\delta t,$$

where

$$\begin{aligned}\vec{k}_1&=\vec{f}(t,\vec{v}(t)),\\ \vec{k}_2&=\vec{f}\left(t+\frac{\delta t}{2},\vec{v}(t)+\vec{k}_1\frac{\delta t}{2}\right),\\ \vec{k}_3&=\vec{f}\left(t+\frac{\delta t}{2},\vec{v}(t)+\vec{k}_2\frac{\delta t}{2}\right),\\ \vec{k}_4&=\vec{f}\big(t+\delta t,\vec{v}(t)+\vec{k}_3\delta t\big).\end{aligned}$$

This conditionally stable explicit numerical scheme enables us to use Graphical Processing Units for high-performance computing. We also reuse variables for decreasing memory storage by setting

$$\begin{aligned}\vec{k}_1&=\vec{f}(t,\vec{v}(t)),\\ \vec{k}_2&=\vec{f}\left(t+\frac{\delta t}{2},\vec{v}(t)+\vec{k}_1\frac{\delta t}{2}\right),\\ \vec{k}_1&=\vec{k}_1+2\vec{k}_2,\\ \vec{k}_3&=\vec{f}\left(t+\frac{\delta t}{2},\vec{v}(t)+\vec{k}_2\frac{\delta t}{2}\right),\\ \vec{k}_2&=\vec{f}\big(t+\delta t,\vec{v}(t)+\vec{k}_3\delta t\big),\\ \vec{v}(t+\delta t)&=\vec{v}(t)+\frac{\vec{k}_1+2\vec{k}_3+\vec{k}_2}{6}\delta t.\end{aligned}$$

The numerical code is programmed using PGI CUDA Fortran Compiler [24] and is performed on NVIDIA Tesla K40c GPU Accelerators with 2880 CUDA GPU cores. Using texture data/memory (see, e.g., [23]) we were able to speed up computations by more than 20%. The longest calculation took 27 h to reach the non-dimensional time instant $t = 50$ in the simulation. The largest 3D grid to fit in the 12 GB GPU memory was between 600 and 700 grid points in each of the three spatial variables. The visualization was done using software packages ParaView [2] and MATLAB [27]. A rigorous numerical analysis for the nonlinear partial differential Eq. (1) with time varying coefficient goes beyond the scope of our work. While linear analysis similar to [6] would be certainly feasible, it would be irrelevant to our computational examples that show strong nonlinear behavior. We justify our numerical approach by providing computational evidence of convergence (Example 1) and by demonstrating existing theoretical results (Examples 2 and 3).

2.2. Radial solutions

Some of our numerical examples are for radial solutions of the Higgs boson equation. This simplification is justified partly by the cosmological principle (see, e.g., [20]) that the universe is homogeneous and isotropic on large scales. The radial form of Eq. (10) is

$$\phi_{tt} - \frac{e^{-2t}}{L^2}\left(\frac{2}{r}\frac{\partial}{\partial r}\phi + \frac{\partial^2}{\partial r^2}\phi\right) + 3\phi_t = \mu^2\phi - \lambda\phi^3, \quad r \in (0,1), \quad t \in (0,T] \tag{17}$$

with boundary conditions

$$\phi_r(0,t) = \phi(1,t) = 0, \quad t \in [0,T]$$

and with initial condition

$$\phi(r,0) = \varphi_0(r), \quad r \in [0,1], \tag{18}$$

$$\phi_t(r,0) = \varphi_1(r), \quad r \in [0,1]. \tag{19}$$

The singularity in Eq. (17) at $r = 0$ is treated using L'Hospital's rule

$$\lim_{r\to 0}\frac{\frac{\partial}{\partial r}\phi(r,t)}{r} = \lim_{r\to 0}\frac{\partial^2\phi(r,t)}{\partial r^2} = \frac{\partial^2\phi(0,t)}{\partial r^2}. \tag{20}$$

At the boundary $r = 0$ symmetry is used for boundary conditions using grid points only from the [0, 1] spatial domain:

$$\begin{aligned}\frac{\partial^2\phi(0,t)}{\partial r^2} &\approx \frac{1}{\delta r^2}\Big(-\frac{1}{12}\phi(-2\delta r) + \frac{4}{3}\phi(-\delta r) - \frac{5}{2}\phi(0) + \frac{4}{3}\phi(\delta r) - \frac{1}{12}\phi(2\delta r)\Big)\\ &= \frac{1}{\delta r^2}\Big(-\frac{5}{2}\phi(0) + \frac{8}{3}\phi(\delta r) - \frac{1}{6}\phi(2\delta r)\Big).\end{aligned}$$

Simulations for the radial Eq. (17) and for the full $(3+1)-$dimensional Eq. (10) produced equivalent results. Below we provide all results obtained from numerical simulations for the full $(3+1)-$dimensional case both for radial and for general solutions.

3. Computational examples

In this section we present several examples for different parameter values of μ, λ and for different initial conditions φ_0 and φ_1. Unless otherwise noted in the examples the grid size in space is $n \times n \times n = 500 \times 500 \times 500$, resulting in uniform grid spacing $\delta x = \delta x = \delta x = 2 \times 10^{-3}$. With $\delta t = 10^{-4}$ the Courant–Friedrichs–Lewy (CFL) condition $|\phi| < \frac{\delta x}{\sqrt{3}\delta t} \approx 11.54$ for stability (see, e.g., [26]) has been satisfied for all times and for each of our simulation examples for the Higgs boson equation. For the scaling factor the value $L = 5$ has been used. For visualization of the solution $\phi(\vec{x},t)$ we use line plots along either the line segment connecting the midpoints of the computational cube's faces parallel to the yz–plane (mid-line parallel to the x-axis) or the diagonal line segment connecting the corners (0, 0, 0) and (1, 1, 1) of the unit cube. The horizontal axis shows ranges [0, 500] and $[0, 900]$, respectively on these line plots due to grid the size $n = 500$ and due to the diagonal line segment's length being $500\sqrt{3} \approx 866 \approx 900$. For initial conditions we mostly use variations of the compactly supported, infinitely smooth bump function often used as test functions in the theory of generalized functions (see, e.g., [14])

$$B\big(\vec{x};\vec{C},R\big) = \begin{cases}\exp\left(\dfrac{1}{R^2} - \dfrac{1}{R^2 - \left|\vec{x}-\vec{C}\right|^2}\right) & \text{if } \left|\vec{x}-\vec{C}\right| < R,\\[2ex] 0 & \text{if } \left|\vec{x}-\vec{C}\right| \geq R\end{cases} \tag{21}$$

with center $\vec{C} = (C_1, C_2, C_3) \in \Omega$ and with radius $0 < R \ll 1$. Here $\left|\vec{x}-\vec{C}\right|$ denotes the euclidean distance between points $\vec{x}$ and $\vec{C}$. Note that these basic bump functions have nonnegative values with maximum value 1.

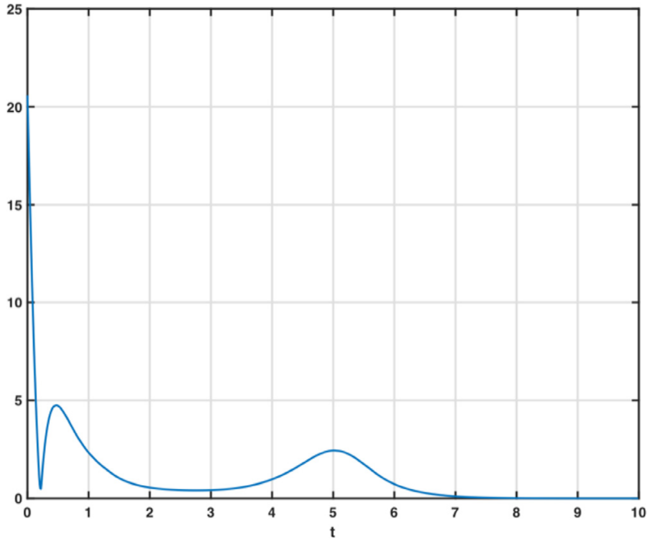

Fig. 1. $\mathcal{P}(t) \equiv \frac{1}{L^2} e^{-2t} \max_{\vec{x}\in\Omega} |\Delta\phi(\vec{x},t)|$.

Example 1. In order to examine the convergence properties of our numerical method we look at an example of Eq. (10) with parameter values $\mu^2 = 9,\ \lambda = 2$ and with the initial conditions

$$\varphi_0(\vec{x}) = 3B(x;\, (0.5, 0.5, 0.5), 0.3), \qquad \forall\vec{x} \in \Omega \tag{22}$$

$$\varphi_1(\vec{x}) = 0, \qquad \forall\vec{x} \in \Omega. \tag{23}$$

This case will be discussed in more details in Example 6. Right now we only look at how the approximate solution changes with respect to different grid sizes and different precisions. We vary the grid size in space and compare the results for values $n = 200,\ 300$, and 400 to the result with $n = 500$ at times $t = 1$ and $t = 2$. Since we are working with compactly supported radial solution starting from a bump function, the solution is nonzero only around the center of the computational domain, and we only consider line plots of the pointwise difference instead of L^2, or other global error norms. Fig. 2 shows stability as the difference between the numerical solutions decreases with increasing values of n. The difference is the largest in the region with high slopes, which moves outward from the center. This indicates that numerical difference in dispersion rates plays an important role, as suggested for example in [7] for the acoustic wave equation. Fig. 3 shows the difference between running our code in single and double precision at times $t = 1$ and $t = 2$. The difference between single and double precision results is not significant, and increases slowly with time. The double precision code required about 80% more run-time than the single precision code and resulted in the same qualitative results as the single precision code.

Example 2. As a second computational example we demonstrate that our numerical code can predict the blow up of the sign-preserving solution for not the Higgs boson equation but for the related Klein–Gordon equation with imaginary mass (see Theorem 1.1 in [30]). For this purpose we set the parameter values to $\mu^2 = 1$ and $\lambda = -1$. As initial conditions we use the bump functions

$$\varphi_0(\vec{x}) = 2B(\vec{x};\, (0.5, 0.5, 0.5), 0.2), \qquad \forall\vec{x} \in \Omega, \tag{24}$$

$$\varphi_1(\vec{x}) = 10B(\vec{x};\, (0.5, 0.5, 0.5), 0.2), \qquad \forall\vec{x} \in \Omega. \tag{25}$$

Parts (a)-(c) of Fig. 4 show the line plot of the solution $\phi(x,\, t)$ for various times. In particularly, we may notice from parts (a) and (b) that from time $t = 0$ to time $t = 2$ the magnitude of the solution stays around 2 while the compact support of the solution becomes larger. After time $t = 2$ the magnitude of solution suddenly increases and it reaches the value of 130 approximately by time $t = 2.97$ (part (c) of Fig. 4). The blow up of the integral $\int_\Omega \phi(\vec{x},t)d\vec{x}$ shortly after time $t = 2.97$ can be observed in part (d) of Fig. 4, demonstrating the theoretical results of Theorem 1.1 from [30].

Example 3. In this example we demonstrate that under certain conditions the solution forms bubbles. For this purpose we reformulate the theoretical results of Corollary 1.4 in [31, page 453]:

Corollary 4. *[31, Corollary 1.4] Bubble forms if the initial data satisfy*

$$\left(\frac{n}{2} + \sqrt{\frac{n^2}{4} + \mu^2}\right)\varphi_0(\vec{x}) + \varphi_1(\vec{x}) < 0 \quad \forall\vec{x} \in \Omega, \tag{26}$$

Difference between numerical solutions along a center line. w_n is the numerical solution for grid size n.

$t=1$ $t=2$

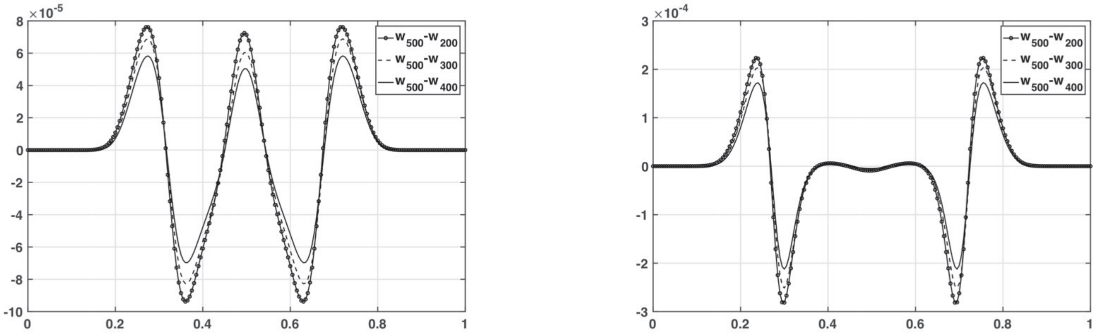

Numerical solution w_{500} along a center line

$t=1$ $t=2$

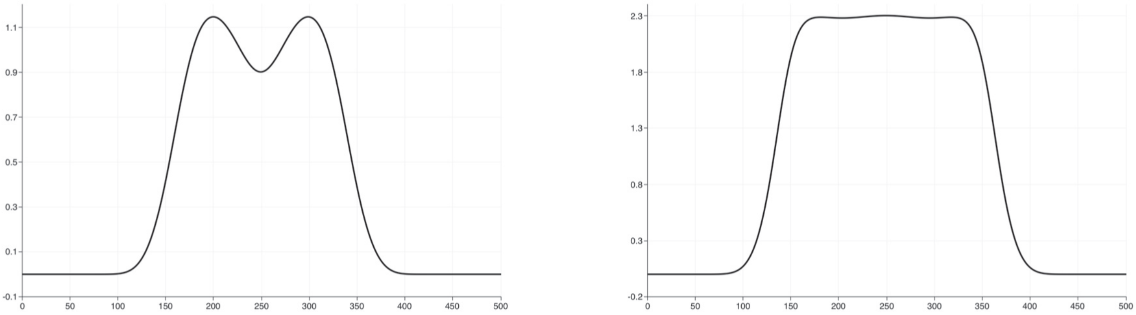

Fig. 2. Convergence of the numerical method.

$t=1$ $t=2$

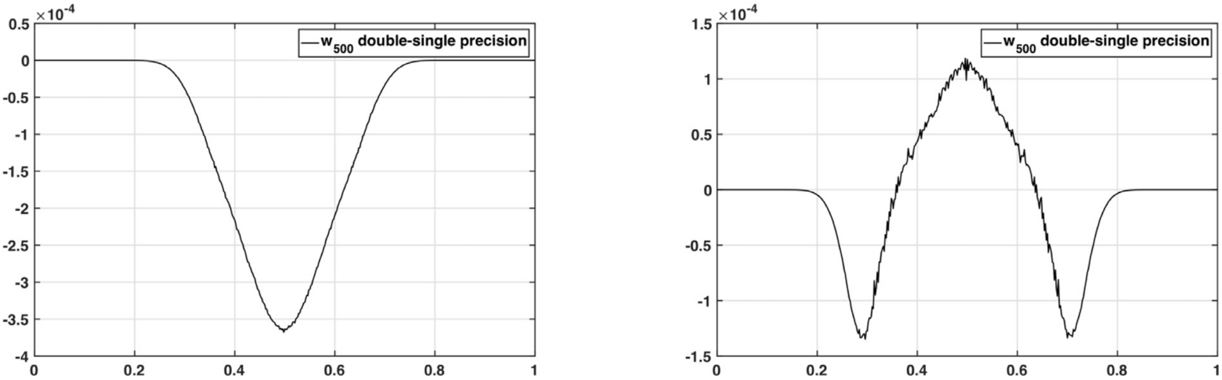

Fig. 3. Difference between double and single precision.

$$\int_{\mathbb{R}^3} \phi^3(\vec{x},t)d\vec{x} \geq 0 \quad \forall t \geq 0. \tag{27}$$

In particular, we consider as initial data the bump functions

$$\varphi_0(\vec{x}) = B\left(\vec{x};\vec{C},r\right), \qquad \forall \vec{x} \in \Omega, \tag{28}$$

$$\varphi_1(\vec{x}) = -5B\left(\vec{x};\vec{C},r\right), \qquad \forall \vec{x} \in \Omega, \tag{29}$$

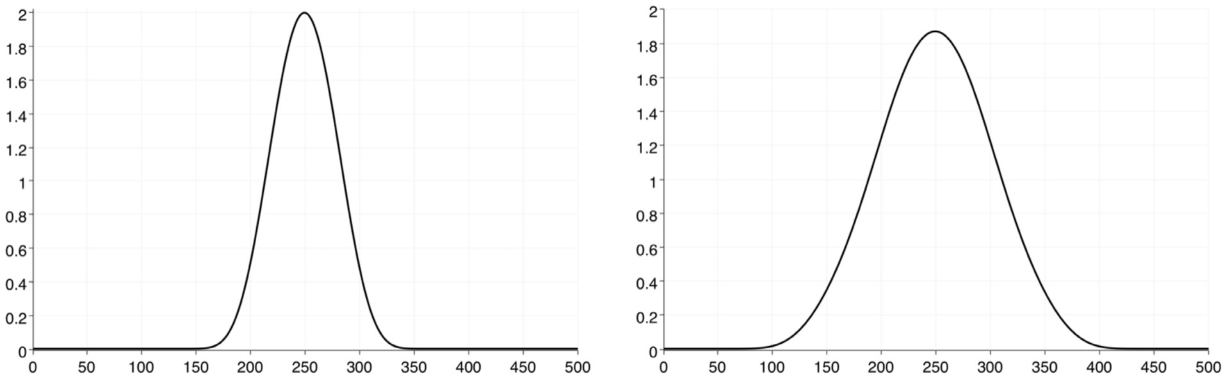
(a) Line plot of solution at $t = 0$

(b) Line plot of solution at $t = 2.0$

(c) Line plot of solution at $t = 2.97$

(d) Blow up of $\int_\Omega \phi(\vec{x}, t)\, d\vec{x}$ around $t = 2.98$

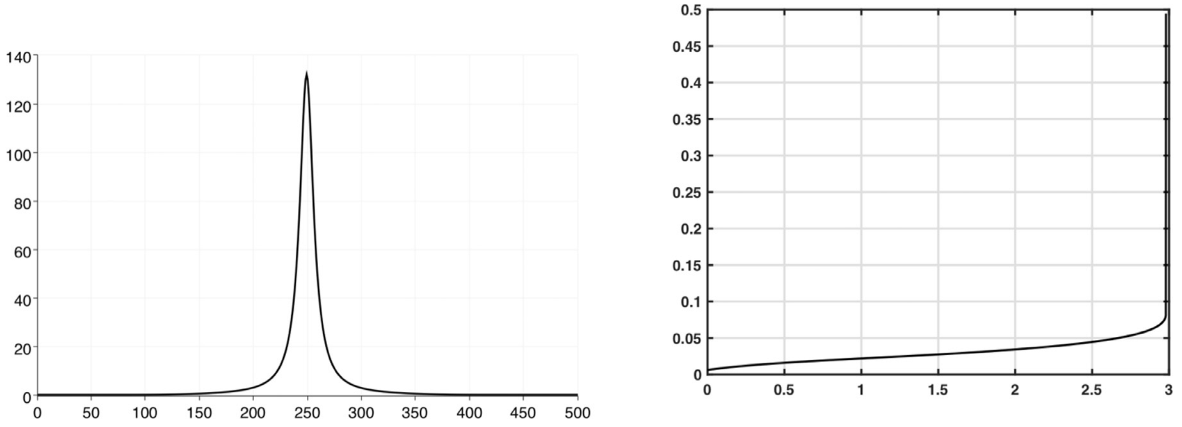

Fig. 4. Blow up of solution to the Klein–Gordon equation with an imaginary mass.

with center $\vec{C} = (0.5, 0.5, 0.5)$ and with radius $r = 0.3$. The line plot of the initial function (28) is depicted in part (a) of Fig. 5. Note that the shift $\vec{x} = \vec{x} - \vec{C}$ makes the initial data and the solution radial. The parameter values are $\mu^2 = 9,\ \lambda = 2$, and hence condition (26) is satisfied inside the domain of support. Condition (27) is also satisfied for $t = 0$ and, by continuity, at least for small $t \geq 0$. On parts (b) and (c) of Fig. 5 for time instances $t = 0.22$ and $t = 0.4$ we can see two points where the solution has zero values with sign change inside the domain of support. These zero places move from the center towards the border of the domain as time goes by. In three space dimensions the isosurface corresponding to these zero values has the shape of a sphere (hence the name bubble) centered at the point $\vec{C} = (0.5, 0.5, 0.5)$, as shown in part (d) of Fig. 5. The radius of the ball increases in time, with the rate of increase decreasing exponentially following the finite speed of propagation $\frac{e^{-t}}{L}$.

We continue this example for larger time in order to investigate the long-time behavior of the solution. Parts (e) and (f) of Fig. 5 show that the solution converges to a piecewise constant (step) function with values 0, 2.12, and −2.12. The step function's shape with sharp corners raises the possibility that the solution looses smoothness. In order to examine the question of differentiability we look at how the quantity $\mathcal{P}(t) \equiv \frac{1}{L^2} e^{-2t} \max_{\vec{x} \in \Omega} |\Delta\phi(\vec{x}, t)|$ (related to the second term from Eq. (10)) changes in time. Fig. 1 shows that the laplacian does not blow up in finite time and hence the solution remains smooth at least up to the second order derivative. Moreover, since $\mathcal{P}(t) \equiv \frac{1}{L^2} e^{-2t} \max_{\vec{x} \in \Omega} |\Delta\phi(\vec{x}, t)|$ converges fast to zero as time t increases, we arrive to the conjecture that Eq. (10) converges to the unforced, damped Duffing equation

$$\phi_{tt} + 3\phi_t = \mu^2\phi - \lambda\phi^3, \quad \vec{x} \in \Omega, \quad t \in (0, T], \tag{30}$$

$$\phi(\vec{x}, 0) = \varphi_0(\vec{x}), \quad \vec{x} \in \Omega, \tag{31}$$

$$\phi_t(\vec{x}, 0) = \varphi_1(\vec{x}), \quad \vec{x} \in \Omega. \tag{32}$$

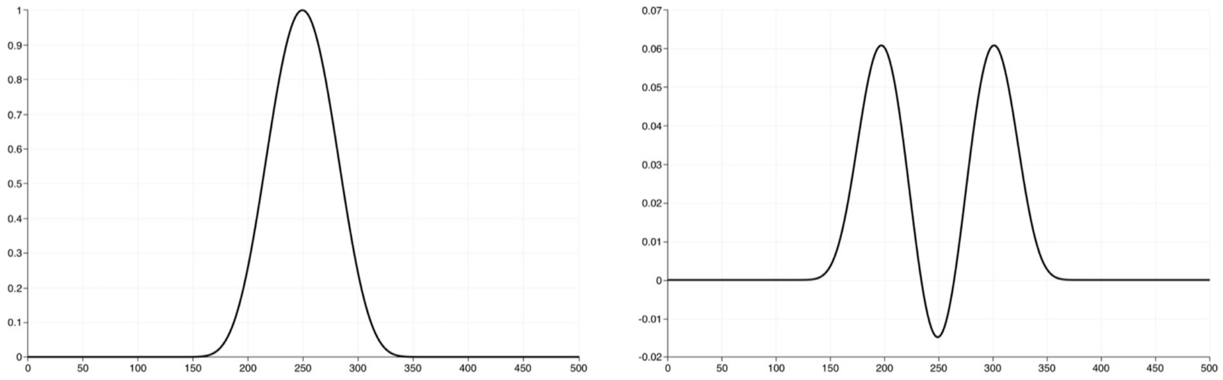

(a) Line plot of solution at $t = 0$

(b) Line plot of solution at $t = 0.22$

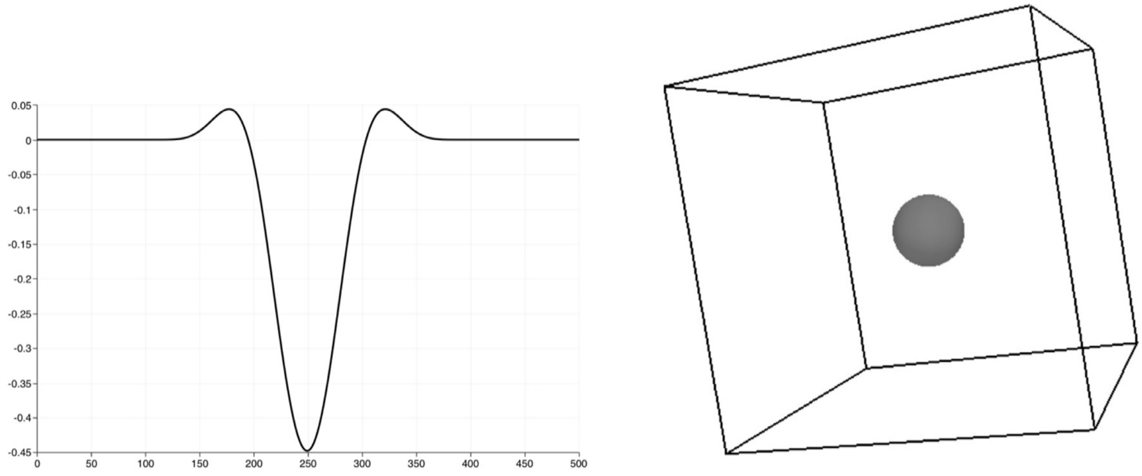

(c) Line plot of solution at $t = 0.4$

(d) 3D bubble at $t = 0.4$

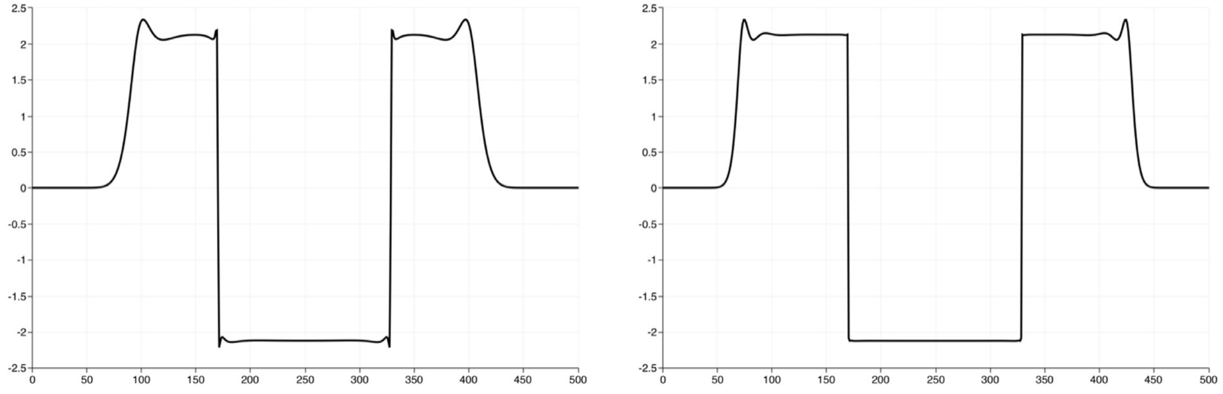

(e) Line plot of solution at $t = 5$

(f) Line plot of solution at $t = 7$

Fig. 5. Bubble formation.

For this ordinary differential equation the two stable equilibrium points are $\pm\sqrt{\frac{\mu^2}{\lambda}} = \pm\sqrt{\frac{9}{2}} \approx \pm 2.12$, and the zero is an unstable equilibrium point. Comparing these values to parts (e)-(f) of Fig. 5 we can observe that after some initial time during which the dissipative term is not negligible, eventually the solution of the Higgs boson Eq. (10) converges to a step function corresponding to the positive and negative equilibrium points of the Duffing Eq. (30). We will discuss the connection with Duffing equations in more details in the next example.

(a) Initial condition in one basin (b) Line plot of solution at time $t = 4$.

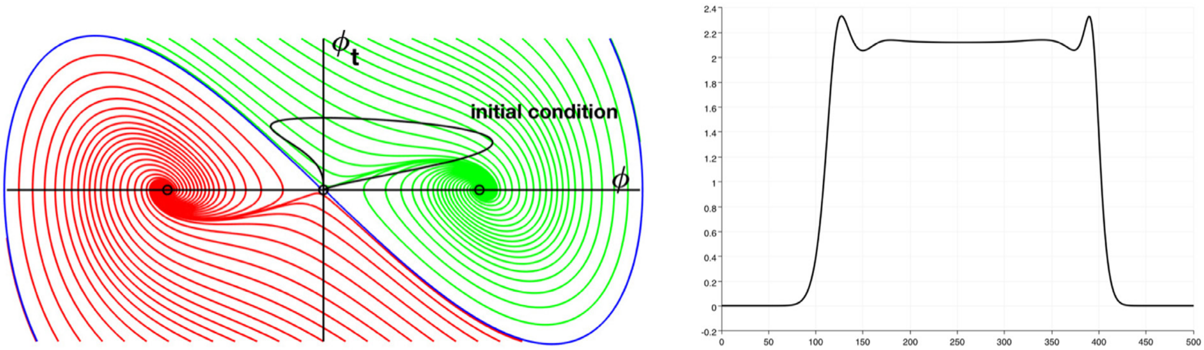

(c) Initial condition across two basins (d) Line plot of solution at time $t = 4$.

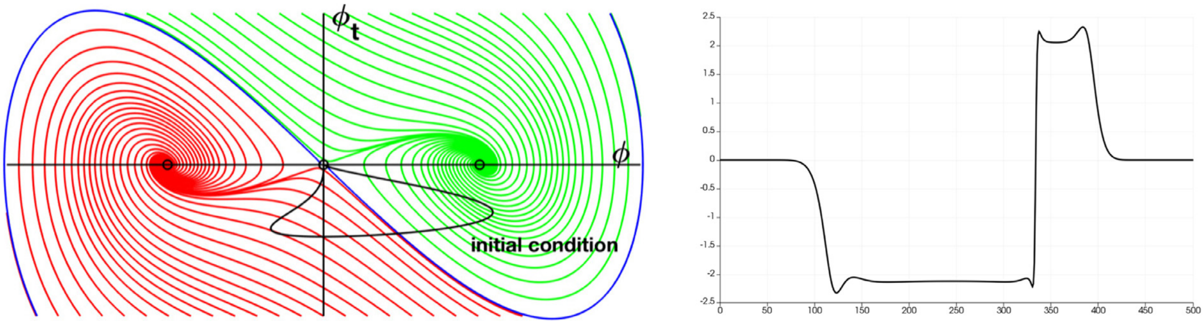

Fig. 6. Convergence to the equilibria of unforced, damped Duffing equation.

Example 5. This example shows a slightly more complicated combination of initial conditions in order to demonstrate the connection between the asymptotic behavior of solutions to the Higgs boson Eq. (10) and the associated damped, unforced Duffing Eq. (30). The parameter values are $\mu^2 = 9,\ \lambda = 2$ as before, and the initial conditions are

$$\varphi_0(\vec{x}) = -10B\big(\vec{x}; \vec{C}_1, r\big)B\big(\vec{x}; \vec{C}_2, r\big)\sin(2\pi x), \quad \forall \vec{x} = (x, y, z) \in \Omega, \tag{33}$$

$$\varphi_1(\vec{x}) = 5B\big(\vec{x}; \vec{C}_1, r\big), \quad \forall \vec{x} \in \Omega, \tag{34}$$

with centers $\vec{C}_1 = (0.5, 0.5, 0.5)$ and $\vec{C}_2 = (0.55, 0.55, 0.55)$ and with radius $r = 0.3$. Note that in the function $\sin(2\pi x)$ of initial condition (33) the variable x is the first component of the thee-dimensional space variable $\vec{x}$. Part (a) of Fig. 6 depicts the curve $(\phi(x, 0.5, 0.5, 0), \phi_t(x, 0.5, 0.5, 0)) = (\varphi_0(x, 0.5, 0.5), \varphi_1(x, 0.5, 0.5))$ for $x \in [0, 1]$ in the phase portrait of the Duffing equation. Note also that this initial data cannot be made radial by a simple shift of the spatial variable. On the other hand, this initial data lies in the damped, unforced Duffing equation's positive equilibrium's basin of attraction (and connects to the unstable zero equilibrium point), even though φ_0 changes sign. Part (a) of Fig. 6 also suggests that the negative part of the initial function φ_0 has to be small relative to the positive part of φ_1 in order for the initial data to stay in the positive equilibrium's basin of attraction. We can observe on the line plot of solution for time $t = 4$ in part (b) of Fig. 6 that the nonzero part of the solution becomes and stays positive for larger time and indeed it converges to the positive equilibrium point $\sqrt{\frac{\mu^2}{\lambda}} = \sqrt{\frac{9}{2}} \approx 2.12$ of the damped, unforced Duffing equation, as expected.

If we modify the initial data (34) to have only non-positive values:

$$\varphi_1(\vec{x}) = -5B(\vec{x}; (0.5, 0.5, 0.5), 0.3), \ \forall \vec{x} \in \Omega. \tag{35}$$

then the curve $(\phi(x, 0.5, 0.5, 0), \phi_t(x, 0.5, 0.5, 0)) = (\varphi_0(x, 0.5, 0.5), \varphi_1(x, 0.5, 0.5))$ for $x \in [0, 1]$ is now split in between the positive and negative equilibria's basin of attraction (see Part (c) of Fig. 6). As a result, some part of the solution converges to the positive equilibrium, while other part converges to the negative equilibrium, whence approaching a step function, which can be observed on the line plot of solution for time $t = 4$ in part (d) of Fig. 6.

Example 6. In this example we demonstrate that under some conditions bubbles do not form. This is a new conjecture supported by our computational result, with currently no theoretical proof existing for it in the literature. The parameter

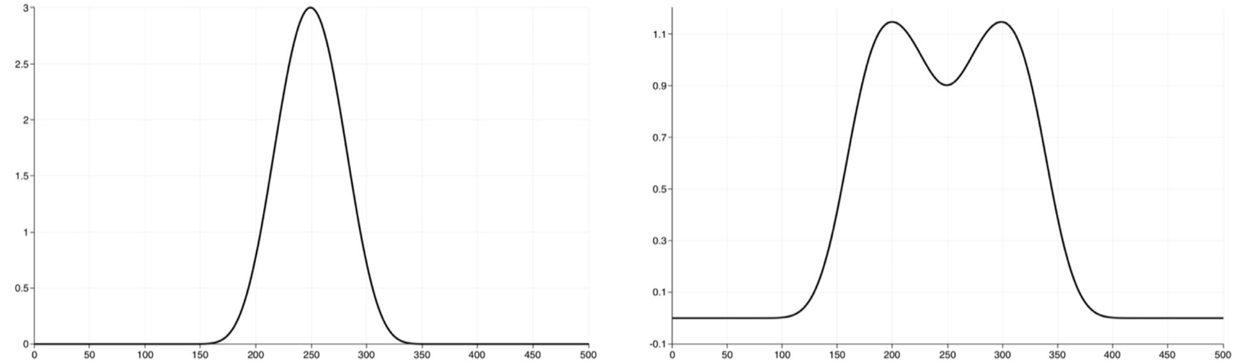
(a) Solution along a line at $t = 0$

(b) Solution along a line at $t = 1$

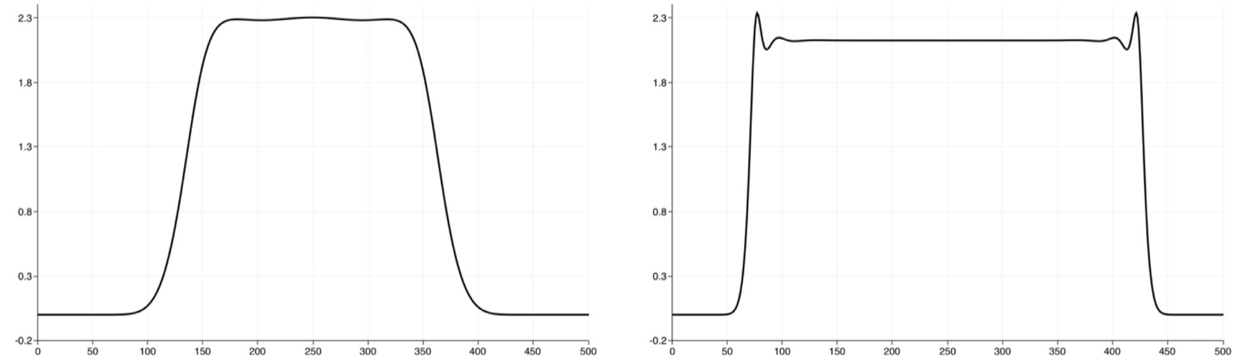
(c) Solution along a line at $t = 2$

(d) Solution along a line at $t = 6$

Fig. 7. Lack of bubble formation.

values are $\mu^2 = 9$, $\lambda = 2$ as before, and the initial conditions are

$$\varphi_0(\vec{x}) = 3B(x;\,(0.5, 0.5, 0.5), 0.3), \qquad \forall \vec{x} \in \Omega \tag{36}$$

$$\varphi_1(\vec{x}) = 0, \qquad \forall \vec{x} \in \Omega. \tag{37}$$

Fig. 7 shows the line plot of the solution for various times. There are no zeros inside the domain of support, which means that no bubbles formed. Note that this initial data lies on the nonnegative horizontal axis of the phase portrait shown in Part (a) of Fig. 6, hence, other than the unstable zero equilibrium, this initial data is in the positive equilibrium's basin of attraction for all $\vec{x}$ in the domain of support. Therefore it should be expected that the solution converges to a step function with values zero and $\sqrt{\frac{\mu^2}{\lambda}} \approx 2.12$, as suggested by the dynamical properties of the corresponding damped, unforced Duffing equation. The main effect the initially non-negligible dissipative term in Eq. (10) seems to have is to propagate the values in space while they converge to the step function's values.

Example 7. In our final example we look at a more complicated scenario with initial conditions that are the sums of two bump functions:

$$\varphi_0(\vec{x}) = B\big(\vec{x}; \vec{C}_1, r\big) + B\big(\vec{x}; \vec{C}_2, r\big), \qquad \forall \vec{x} \in \Omega, \tag{38}$$

$$\varphi_1(\vec{x}) = -5\varphi_0(\vec{x}), \qquad \forall \vec{x} \in \Omega, \tag{39}$$

with centers $\vec{C}_1 = (0.4, 0.4, 0.4)$ and $\vec{C}_2 = (0.6, 0.6, 0.6)$ and with radius $r = 0.2$. The parameter values are $\lambda = \mu^2 = 0.1$. The first initial data $\varphi_0(\vec{x})$ in this case cannot be made radial by a simple shift in the spatial variable. Initially the dissipative term is large compared to the speed at which the solution converges to the Duffing equation's step function. As a result, two bubbles form and they interact with each other. For line plots we used the main diagonal line segments of the computational cube, since the centers of the initial conditions's bump functions are on that diagonal. Figs. 8–10 show the formation and interactions of bubbles. Initially there is no bubble present. After the two bubbles form at around $t = 0.08$ (parts (a.1) and (a.2) of Fig. 8), their size grows continuously in time (parts (b.1) and (b.2) of Fig. 8). Around time $t = 0.69$ the two bubbles touch (parts (c.1) and (c.2) of Fig. 8), and from that time on they are attached to each other. At time $t = 0.8$ (shown on

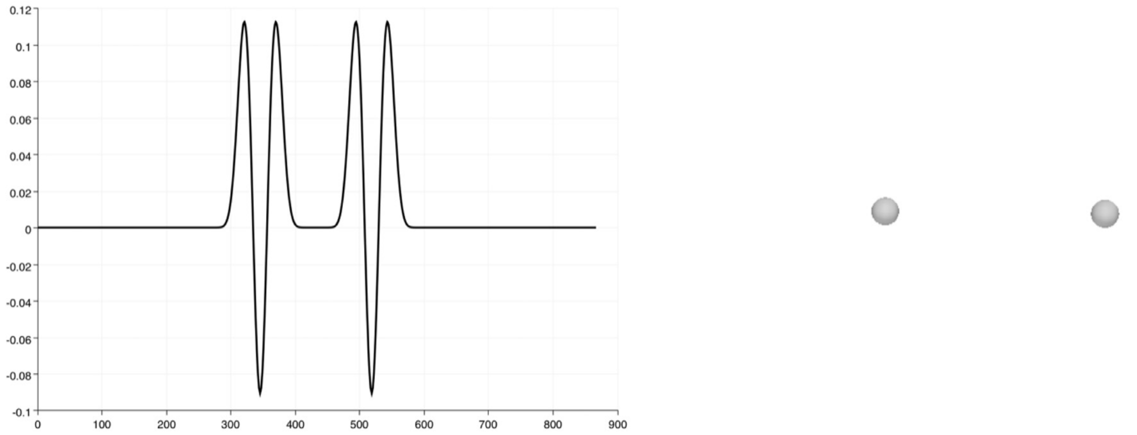
(a.1) Solution along a line at $t = 0.08$

(a.2) 3D bubbles at $t = 0.08$

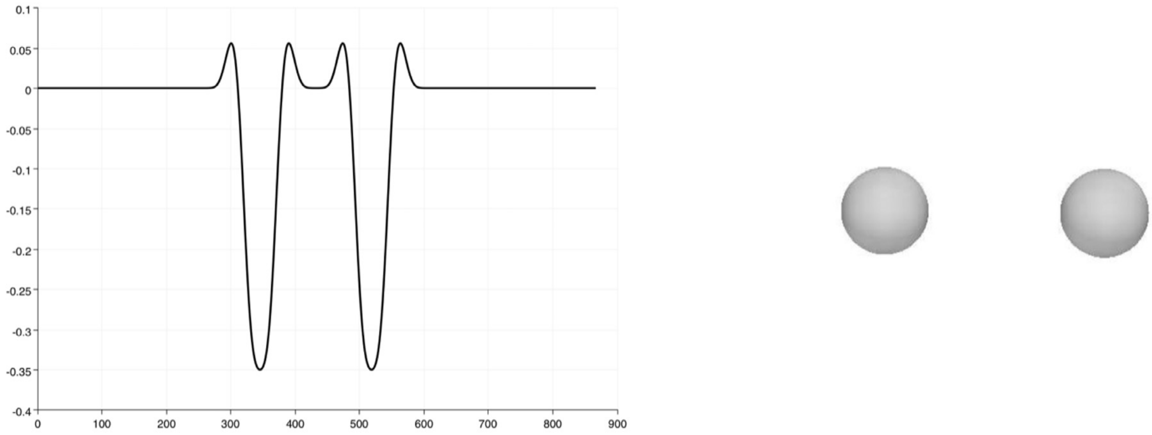
(b.1) Solution along a line at $t = 0.2$

(b.2) 3D bubbles at $t = 0.2$

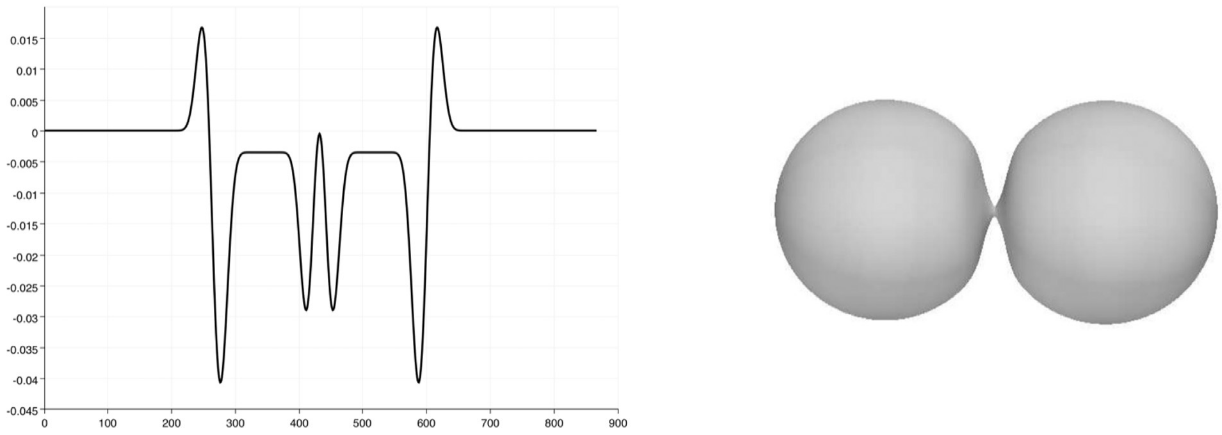
(c.1) Solution along a line at $t = 0.69$

(c.2) 3D bubbles at $t = 0.69$

Fig. 8. Interaction of two bubbles I.

(a.1) Solution along a line at $t = 0.8$ (a.2) 3D bubbles at $t = 0.8$

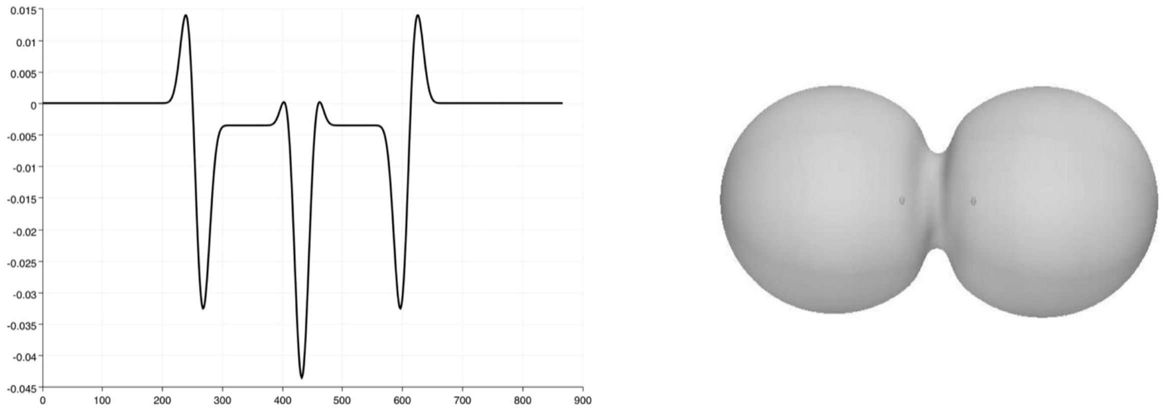

(b.1) Solution along a line at $t = 1$ (b.2) 3D bubbles at $t = 1$

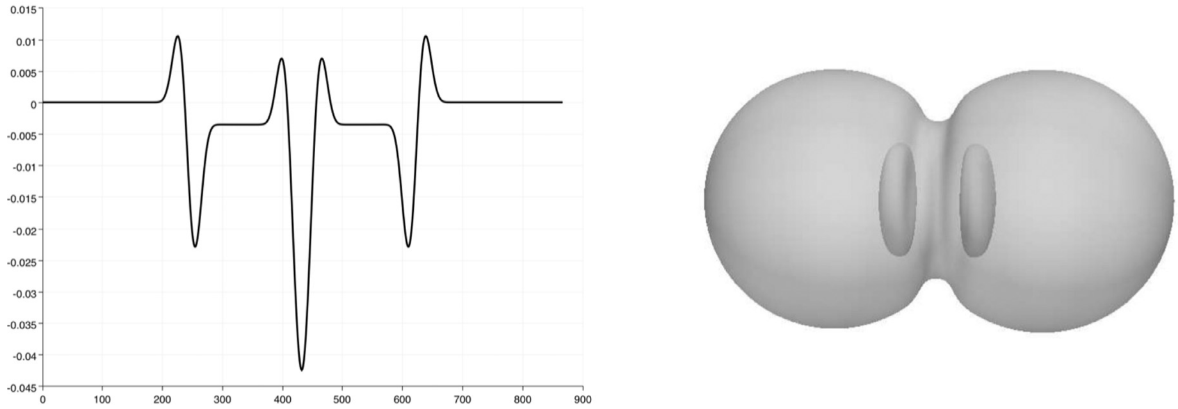

(c.1) Solution along a line at $t = 2$ (c.2) 3D bubbles at $t = 2$

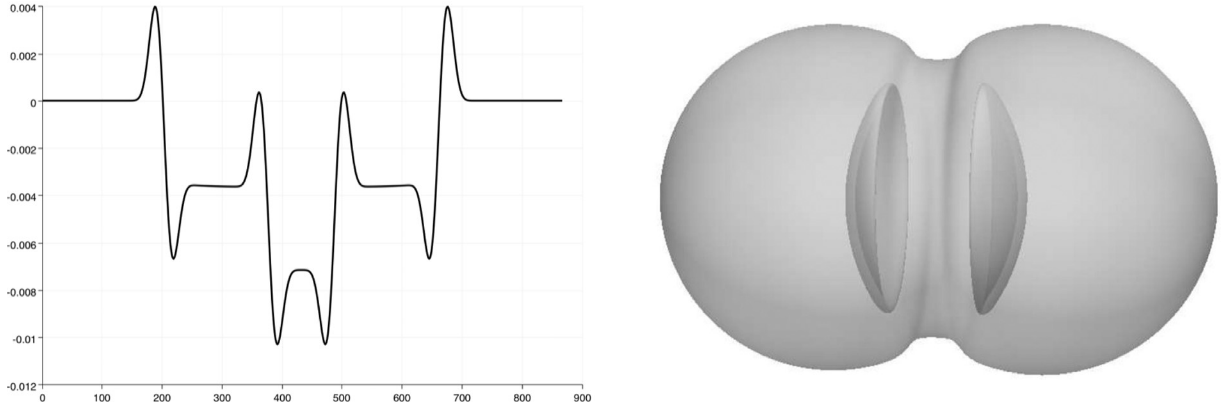

Fig. 9. Interaction of two bubbles II.

parts (a.1) and (a.2) of Fig. 9) an additional, tiny bubble forms inside each of the now merged bubbles. These additional bubbles grow (parts (b.1) and (b.2) of Fig. 9 at time $t = 1$); then they flatten and become concave (part (c.1) and (c.2) of Fig. 9 at time $t = 2$). Later hole forms in these inner bubbles, and they become toroidal (parts (a.1) and (a.2) of Fig. 10 at time $t = 2.15$). Finally they disappear (parts (b.1) and (b.2) of Fig. 10 at time $t = 3$). The growth of the larger outer bubble exponentially slows down and it does not seem to change its shape after time $t = 3$. Parts (c.1) and (c.2) of Fig. 10 show the

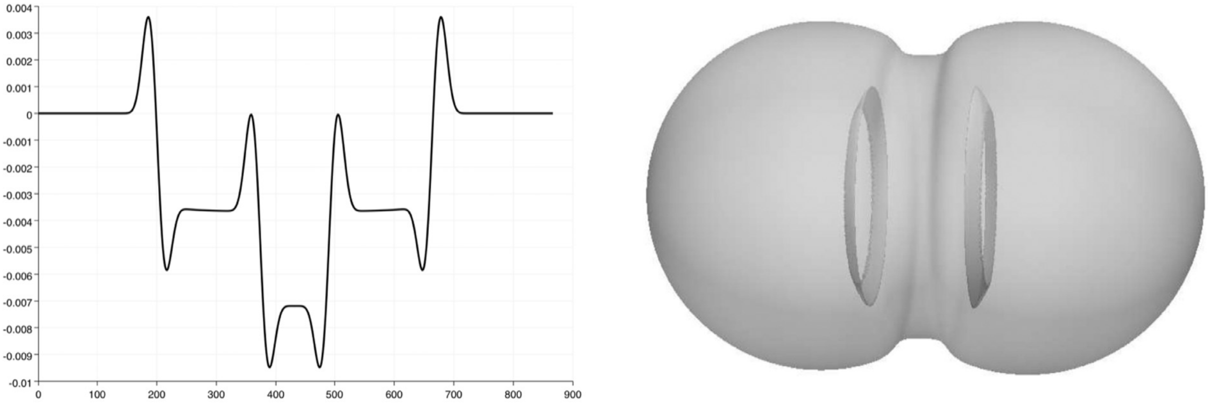
(a.1) Solution along a line at $t = 2.15$ (a.2) 3D bubbles at $t = 2.15$

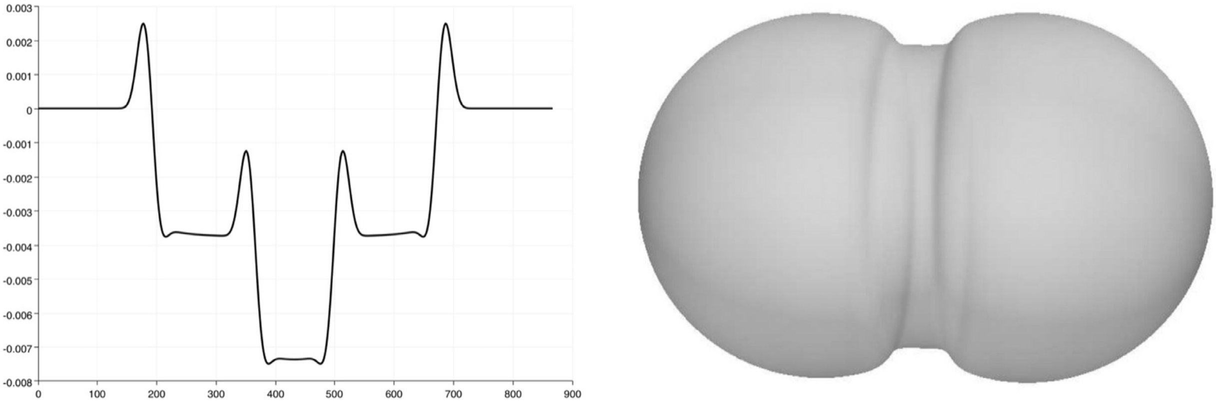
(b.1) Solution along a line at $t = 3$ (b.2) 3D bubbles at $t = 3$

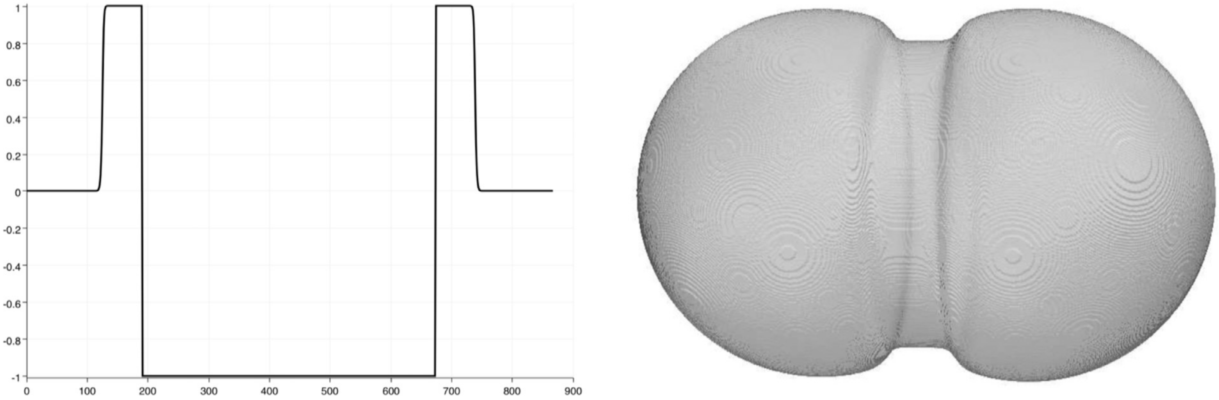
(c.1) Solution along a line at $t = 50$ (c.2) 3D bubbles at $t = 50$

Fig. 10. Interaction of two bubbles III.

bubble in a quasi-steady state due to the dissipative term in Eq. (10) being very close to zero and the solution very close to the step function with constant values 0 and $\pm\sqrt{\frac{\mu^2}{\lambda}} = \pm 1$ of the corresponding damped, unforced Duffing equation's equilibrium points.

4. Conclusion

In this paper, we examined numerical solutions of the Higgs boson equation in the de Sitter spacetime. Our approach was based on a fourth order finite difference method in space and an explicit fourth order Runge-Kutta method in time for the discretization. High performance computations performed using NVIDIA Tesla K40c GPU Accelerators demonstrated existing theoretical results and suggested several previously not known properties of the solution for which theoretical proofs do not exist yet. Namely, we conjecture that for smooth initial conditions a smooth solution exists globally for all time; under some initial conditions no bubbles form (depending on the position of initial data in the basin of attractions of the unforced, damped Duffing equation's stable equilibrium points); and solutions converge to step functions determined by the initial conditions and related to unforced, damped Duffing equations. The theoretical proofs of these conjectures is in our future plan, as well as to investigate and mitigate the numerical difficulty to correctly simulate the places where sharp corners develop in the solution. Remarkably, despite the sharp corners, our numerical method did not break down for the time intervals considered.

Acknowledgments

The authors are indebted to the anonymous referees for the remarks and suggestions, which improved the readability of the text. The authors acknowledge the Texas Advanced Computing Center (TACC) at The University of Texas at Austin for providing high performance computing and visualization resources that have contributed to the research results reported within this paper. URL: http://www.tacc.utexas.edu. We also gratefully acknowledge the support of NVIDIA Corporation with the donation of the Tesla K40 GPU used for this research. K. Yagdjian was supported by University of Texas Rio Grande Valley College of Sciences 2016-17 Research Enhancement Seed Grant.

References

[1] Adams RA, Fournier JJF. Sobolev spaces. Pure and applied mathematics (Amsterdam), 140. 2nd. Amsterdam: Elsevier/Academic Press; 2003. ISBN 0-12-044143-8.

[2] Ayachit U. The paraview guide: a parallel visualization application. USA: Kitware, Inc.; 2015. ISBN 1930934300, 9781930934306.

[3] Basak KC, Ray PC, Bera RK. Solution of non-linear Klein–Gordon equation with a quadratic non-linear term by Adomian decomposition method. Commun Nonlinear Sci Numer Simul 2009;14(3):718–23. doi:10.1016/j.cnsns.2007.09.018. http://www.sciencedirect.com/science/article/pii/S1007570407002845.

[4] Bers A, Fox R, Kuper CG, Lipson SG. The impossibility of free tachyons. In: Kuper CG, Peres A, editors. Relativity and gravitation. New York: Gordon and Breach Science Publishers; 1971. p. 41–6.

[5] Bogey C, Bailly C. A family of low dispersive and low dissipative explicit schemes for flow and noise computations. J Comput Phys 2004;194(1):194–214. doi:10.1016/j.jcp.2003.09.003. http://www.sciencedirect.com/science/article/pii/S0021999103004662.

[6] Caplan R, Carretero-González R. Numerical stability of explicit Runge–Kutta finite-difference schemes for the nonlinear Schrödinger equation. Appl Numer Math 2013;71:24–40. doi:10.1016/j.apnum.2013.04.002. http://www.sciencedirect.com/science/article/pii/S0168927413000627.

[7] Cohen G, Joly P. Construction and analysis of fourth-order finite difference schemes for the acoustic wave equation in nonhomogeneous media. SIAM J Numer Anal 1996;33(4):1266–302. http://www.jstor.org/stable/2158304.

[8] Coleman S. Aspects of symmetry: selected Erice lectures. Cambridge University Press; 1985. doi:10.1017/CBO9780511565045.

[9] Dehghan M, Mohebbi A, Asgari Z. Fourth-order compact solution of the nonlinear Klein–Gordon equation. Numer Algorithms 2009;52(4):523. doi:10.1007/s11075-009-9296-x.

[10] Dehghan M, Shokri A. Numerical solution of the nonlinear Klein–Gordon equation using radial basis functions. J Comput Appl Math 2009;230(2):400–10. doi:10.1016/j.cam.2008.12.011. http://www.sciencedirect.com/science/article/pii/S0377042708006365.

[11] Dekker K, Verwer J. Stability of Runge–Kutta methods for stiff nonlinear differential equations. North-Holland, Amsterdam: Elsevier Science Ltd; 1984.

[12] Donninger R, Schlag W. Numerical study of the blowup/global existence dichotomy for the focusing cubic nonlinear Klein–Gordon equation. Nonlinearity 2011;24(9):2547. http://stacks.iop.org/0951-7715/24/i=9/a=009.

[13] Epstein H, Moschella U. De sitter tachyons and related topics. Comm Math Phys 2015;336(1):381–430. doi:10.1007/s00220-015-2308-x.

[14] Fry R, McManus S. Smooth bump functions and the geometry of Banach spaces: a brief survey. Expo Math 2002;20(2):143–83. doi:10.1016/S0723-0869(02)80017-2. http://www.sciencedirect.com/science/article/pii/S0723086902800172.

[15] Griffiths G, Schiesser W. Traveling wave analysis of partial differential equations: numerical and analytical methods with matlab and maple. Elsevier Science; 2010. ISBN 9780123846532. https://books.google.com/books?id=c_PZIw-cl_cC.

[16] Hörmander L. Lectures on nonlinear hyperbolic differential equations. Mathématiques & Applications [Mathematics & Applications], 26. Berlin: Springer-Verlag; 1997. ISBN 3-540-62921-1.

[17] Jiménez S, Vázquez L. Analysis of four numerical schemes for a nonlinear Klein–Gordon equation. Appl Math Comput 1990;35(1):61–94. http://www.sciencedirect.com/science/article/pii/009630039090091G.

[18] Kaya D, El-Sayed SM. A numerical solution of the Klein–Gordon equation and convergence of the decomposition method. Appl Math Comput 2004;156(2):341–53. doi:10.1016/j.amc.2003.07.014. http://www.sciencedirect.com/science/article/pii/S0096300303008531.

[19] Keller HB, Pereyra V. Symbolic generation of finite difference formulas. Math Comp 1978;32(144):955–71. doi:10.2307/2006328.

[20] Liddle A. An introduction to modern cosmology. 3. Wiley; 2015. ISBN 9781118502143. http://amazon.com/o/ASIN/1118502140/.

[21] Linde AD. Particle physics and inflationary cosmology. Chur Switzerland New York: Harwood Academic Publishers; 1990. ISBN 978–3718604906.

[22] Macías-Díaz J, Jerez-Galiano S. Two finite-difference schemes that preserve the dissipation of energy in a system of modified wave equations. Commun Nonlinear Sci Numer Simul 2010;15(3):552–63. doi:10.1016/j.cnsns.2009.04.017. http://www.sciencedirect.com/science/article/pii/S1007570409002056.

[23] NVIDIA Corporation. CUDA fortran programming guide and reference. https://www.pgroup.com/doc/pgicudaforug.pdf; 2017b.

[24] NVIDIA Corporation. PGI CUDA Fortran compiler. http://www.pgroup.com/resources/cudafortran.htm; 2017a.

[25] Rashidinia J, Ghasemi M, Jalilian R. Numerical solution of the nonlinear Klein–Gordon equation. J Comput Appl Math 2010;233(8):1866–78. doi:10.1016/j.cam.2009.09.023. http://www.sciencedirect.com/science/article/pii/S0377042709006451.

[26] Strang G. Computational science and engineering. Wellesley, MA: Wellesley-Cambridge Press; 2007. ISBN 978-0-9614088-1-7; 0-9614088-1-2.

[27] The MathWorks Inc. MATLAB and Statistics Toolbox Release 2017b. https://www.mathworks.com/; 2017.

[28] van der Houwen PJ. The development of Runge–Kutta methods for partial differential equations. Appl Numer Math 1996;20(3):261–72. doi:10.1016/0168-9274(95)00109-3.

[29] Voronov NA, Dyshko L, Konyukhova NB. On the stability of a self-similar spherical bubble of a scalar Higgs field in de sitter space. Phys At Nucl 2005;68(7):1218–26. doi:10.1134/1.1992577.

[30] Yagdjian K. The semilinear Klein-Gordon equation in de sitter spacetime. Discrete Contin Dyn Syst Ser-S 2009;2(3):679–96. doi:10.3934/dcdss.2009.2.679.

[31] Yagdjian K. On the global solutions of the higgs boson equation. Communications in Partial Differential Equations 2012;37(3):447–78. doi:10.1080/03605302.2011.641052.

[32] Yagdjian K. Global existence of the self-interacting scalar field in the de Sitter universe, https://arxiv.org/abs/1706.07703.

[33] Yazici M, Şengül S. Approximate solutions to the nonlinear Klein–Gordon equation in de Sitter spacetime. Open Phys. 2016;14(1):314–20. doi:10.1515/phys-2016-0037.